



# Effect of Substrate Surface Roughness on Microstructure and Mechanical Properties of Cold-Sprayed Ti6Al4V Coatings on Ti6Al4V Substrates

Adrian Wei-Yee Tan<sup>1,2</sup> · Wen Sun<sup>1,2</sup> · Ayan Bhowmik<sup>1,2</sup> · Jun Yan Lek<sup>3</sup> · Xu Song<sup>4</sup> · Wei Zhai<sup>5</sup> · Han Zheng<sup>2,5</sup> · Feng Li<sup>1,6</sup> · Iulian Marinescu<sup>1,6</sup> · Zhili Dong<sup>7</sup> · Erjia Liu<sup>1,2</sup>

Submitted: 4 June 2019 / in revised form: 30 July 2019 / Published online: 30 October 2019  
© ASM International 2019

**Abstract** Surface condition, especially surface roughness of substrates, critically influences the adhesion of cold-sprayed titanium alloy coatings. To study this, Ti6Al4V (Ti64) coatings were deposited on Ti64 substrates with increasing surface roughness ( $R_a$ ) from 0.05  $\mu\text{m}$  (polished surface) to 5.4  $\mu\text{m}$  (water-jet cut surface). It was found that the substrate surface roughness did not significantly affect the porosity, hardness and coating surface roughness because these properties were dependent on the deposition parameters such as propellant gas pressure and temperature and nozzle traverse speed. The adhesion test results showed that smoother substrate surfaces improved the coating bond strength of the cold-sprayed Ti64 coatings from about 7.1 MPa ( $R_a$ : 5.4  $\mu\text{m}$ , interface failure) to 68.7 MPa ( $R_a$ : 0.05  $\mu\text{m}$ , glue failure). The fracture characteristics of the debonded coating/substrate interfaces revealed that there were more adiabatic shear-induced craters observed on the smoother substrate surfaces. Finite element modeling also

showed that the substrate surface features (i.e., peaks and valleys) possibly prevented the intimate contact between the particles and substrate and thus induced the non-uniform distributions of temperature, stress and strain at the particle/substrate interface.

**Keywords** finite element analysis · high-pressure cold spray · mechanical properties · substrate surface condition · Ti6Al4V powder/coating/substrate

## Introduction

Ti6Al4V (Ti64) is a particularly attractive alloy for high-performance structural applications due to its high specific strength, low density, high corrosion resistance and great thermal stability up to 400 °C (Ref 1). However, aerospace components made of Ti64 often suffer from wear, erosion and tear over their service periods due to harsh operation conditions. Repair of the damaged Ti64 components is

**Electronic supplementary material** The online version of this article (<https://doi.org/10.1007/s11666-019-00926-5>) contains supplementary material, which is available to authorized users.

✉ Adrian Wei-Yee Tan  
adriantan@ntu.edu.sg

✉ Erjia Liu  
mejliu@ntu.edu.sg

<sup>1</sup> Rolls-Royce@NTU Corporate Lab, Nanyang Technological University, 50 Nanyang Avenue, Singapore 639798, Singapore

<sup>2</sup> School of Mechanical and Aerospace Engineering, Nanyang Technological University, 50 Nanyang Avenue, Singapore 639798, Singapore

<sup>3</sup> Facility for Analysis, Characterisation, Testing and Simulation (FACTS), Nanyang Technological University, Singapore 639798, Singapore

<sup>4</sup> School of Mechanical and Automation Engineering, Chinese University of Hong Kong, William M.W. Mong Engineering Building, Shatin, Hong Kong

<sup>5</sup> Singapore Institute of Manufacturing Technology (SIMTech), 73 Nanyang Drive, Singapore 637662, Singapore

<sup>6</sup> Central Technology Group, Rolls-Royce Singapore Pte Ltd, 1 Seletar Aerospace Crescent, Singapore 797575, Singapore

<sup>7</sup> School of Materials Science and Engineering, Nanyang Technological University, 50 Nanyang Avenue, Singapore 639798, Singapore

critical and challenging for the aerospace industry due to their high raw material and manufacturing costs.

Cold spray (CS) emerges to be a potential repair technique for Ti64 components, due to its low processing temperature with minimum sample distortion, as compared to conventional repair processes such as thermal spray and welding. Cold spray is a material deposition process where particles are accelerated to supersonic speed and impact on the target substrate surface to form a dense coating in solid state (Ref 2-10). Several factors that would influence CS Ti64 coating quality are substrate surface conditions [temperature, roughness, hardness (Ref 11-14)], particle type and size (Ref 15), impact angle, velocity (Ref 16-18) and temperature (Ref 19), coating thickness (Ref 20, 21), as well as post-processes such as heat treatment (Ref 22, 23).

The substrate surface preparation of the damaged parts is critical to ensure strong adhesion of the cold-sprayed Ti64 coatings in order to meet the strict operational demands. It has been mentioned that substrates prior to CS do not require surface preparations as the impacts from the particles tend to provide cleaning (oxide removal and degreasing) and roughening (erosion). However, experimental results have revealed that the surface condition of substrates (roughness or heated) greatly affects the coating qualities, especially coating adhesion strength (Ref 12, 13, 24-29). The correlation of substrate surface condition effect with adhesion strength is a complicated issue as it is dependent on the material combination of particle-substrate as well as the process parameters for particle deposition.

One of the theories suggested increasing substrate surface roughness promotes mechanical interlocking of the impinging powder particles to the substrate surface. High substrate surface roughnesses have shown to promote adhesion strength and deposition efficiency for ductile coatings such as Cu, pure Ti and Al (Ref 24, 30-34). Particles would have extra sites on the substrate to interlock with. On the other hand, for a substrate surface with a low roughness, there would be fewer surface areas for the particles to bind upon impact, which might result in a lower bond strength. In addition, as these particles have difficulty to adhere well, the deposition efficiency would be reduced as well.

However, a smoothly polished surface, for example, to mirror-like condition, has also proven to improve coating adhesion strength for some materials such as CS Ti and Ti64 coatings. This surface condition provides an intimate oxide-free platform for strong metallurgical bonding. Marrocco et al. (Ref 30) observed that increasing roughness by grit-blasting surfaces lowers the bond strength of bonding of Ti coating on the Ti64 substrate. It is suspected that the Ti64 substrate was work-hardened by grit-blasting process. This results in less substrate deformation and effective surface oxide removal by the impact of Ti particles during

CS process. On the other hand, a higher adhesion strength was also reported for the case of CS pure Ti splats on a smoother  $\text{Al}_2\text{O}_3$  ceramic surface, where bonding occurs along the periphery of the particle where jetting occurs (Ref 28). This trend generally has also been observed by other Ti depositions onto various rough surfaces shown in Table 1.

Perton et al. (Ref 11) showed that CS Ti64 coatings deposited on smoother Ti64 surfaces (mirror-like) could achieve a higher adhesion strength [measured by laser shock adhesion test (LASAT)]. Although increasing the substrate surface roughness yielded a greater surface contact area for adhesion, but due to lower deformability of the Ti64 particles during CS, they failed to fill the asperities created by the roughening procedure. However, as the size of asperities increased, the particles filled in these asperities better and the true actual surface contact increased, leading to an increase in coating adhesive strength. However, there is a lack of in-depth study of the microstructure and fracture pattern of CS Ti64 coatings, which can improve the understanding.

In this work, we investigated the effects of different Ti64 substrate surface roughnesses, smooth ( $R_a$ : 0.05  $\mu\text{m}$ ) to rough ( $R_a$ : 5.4  $\mu\text{m}$ ), on the quality of cold-sprayed Ti64 coatings. The coatings were evaluated in terms of porosity, microstructure, hardness, and adhesion strength, through experimental evaluation and FEM modeling.

## Experimental Method

### Materials

Ti64 (grade 5) disks (Titan Engineering, Singapore) with dimensions of 25 mm diameter  $\times$  5 mm thickness were used as substrates. Four types of substrate surface roughness ( $R_a$ ) were prepared, i.e., 0.05, 0.3, 2.2 and 5.4  $\mu\text{m}$  using polishing (with #1200 grit SiC foil), grinding wheel, sand-blasting (alumina) and water-jet cutting (as-received condition), respectively. The analyses of the substrate surfaces are shown in “[Substrate Surface Analysis](#)” section. The substrates were degreased before cold spray deposition. The Ti64 powders used are plasma-atomized and spherical in-shape from AP&C Canada (Fig. 1). The average size of the powders ranges from 15 to 25  $\mu\text{m}$  and the powders have a mean hardness of 386 HV (Ref 38).

### Cold Spray Process

All Ti64 coatings were deposited using an Impact Spray system (5/11, Impact Innovations, Germany). The deposition details are shown in Table 2. The details of the nozzle

dimension and spraying procedure have been reported elsewhere by Tan et al. (Ref 16, 39). The measured particle velocity using Tecnar Cold Spray Meter was around  $780 \text{ ms}^{-1}$ . For easy reference, the coatings deposited on the substrates with the surface roughnesses ( $R_a$ ) of 0.05, 0.3, 2.2 and  $5.4 \mu\text{m}$  were referred to as S1, S2, S3 and S4, respectively.

**Microstructural and Mechanical Characterization**

The surface roughnesses  $R_a$  and  $R_z$  of the substrates and the as-sprayed coatings were measured (averaged over three readings per sample) with a contact mode surface profilometer (Talyscan 150, Taylor Hobson, USA) with a  $4\text{-}\mu\text{m}$ -diameter tip. The measurements were performed with a scan length of 30 mm, a step size of  $1 \mu\text{m}$  and a scan speed of  $1 \text{ mm/s}$ .

For the cross-sectional analysis, each cold-sprayed sample was cut into halves with the dimensions of 25 mm (length)  $\times$  6.5 to 7 mm (thickness). The cut samples were

mounted, and ground with #320 grit SiC foil, followed by chemical–mechanical polishing (CMP) with a DiaPro solution containing  $9 \mu\text{m}$  diamond particles and then an OP-S suspension solution containing  $0.04 \mu\text{m}$  colloidal silica particles (Struers, Denmark). The polished samples were etched for the microstructural evaluation using Kroll’s reagent by immersion method for 10 to 15 s.

Microstructures and porosities of the samples were observed under optical microscopy (OM, Axioskop 2 MAT, Carl Zeiss, Germany) and/or scanning electron microscopy (SEM, JSM-5600LV JEOL, USA) operated at 15 to 20 kV. For the porosity measurement, a series of 16 continuous cross-sectional images (optical micrographs with  $200\times$  magnification) were taken from the coating top, middle and near-interface regions. These images were stitched (per location) and processed using an open-source software called ImageJ (NIH, USA) (Ref 40).

Microhardness of each sample was evaluated using a Vickers microindenter (FM-300e, Future-Tech, Japan) with a 300 g load. A total of ten indents were randomly made

**Table 1** Comparison of surface preparation and bond strength

Author (et al.)	Ref.	Coating	Substrate	Surface preparation	$R_a, \mu\text{m}$	Adhesion strength, MPa
Wang	35	Ti	Mild steel	Grit-blasted	...	8-16
Imbriglio	28	Ti splats	$\text{Al}_2\text{O}_3$	Polished	$0.16 \pm 0.03\text{(c)}$	$305 \pm 87\text{(b)}$
				As-received	$0.78 \pm 0.38\text{(c)}$	$237 \pm 47\text{(b)}$
Li	36	Ti	Mild steel	Grit-blasted	...	$15 \pm 4$
Bae	9	Ti	Mild steel	Grit-blasted	...	50-85
Marroco	30	Ti	Ti64	Polished	$0.046 \pm 0.002$	23
				Ground	$0.21 \pm 0.03$	22
				Grit-blasted	$2.66 \pm 0.06$	7
Price	37	Ti	Ti64	As-received	$\sim 2.6$	37
				Grit-blasted	$\sim 3.5$	32
Perton	11	Ti64	Ti64	Mirror	0.05	$> 80/900\text{(a)}$
				As-machined	2.56	$41/70\text{(a)}$
				Grit 24	5.53	$> 80/371\text{(a)}$

(a) Laser shock adhesive tester; (b) scratch tester; (c) measured in  $R_{pk}$ ; reduced peak height value

**Fig. 1** SEM micrographs of Ti64 grade 5 powder with different magnifications

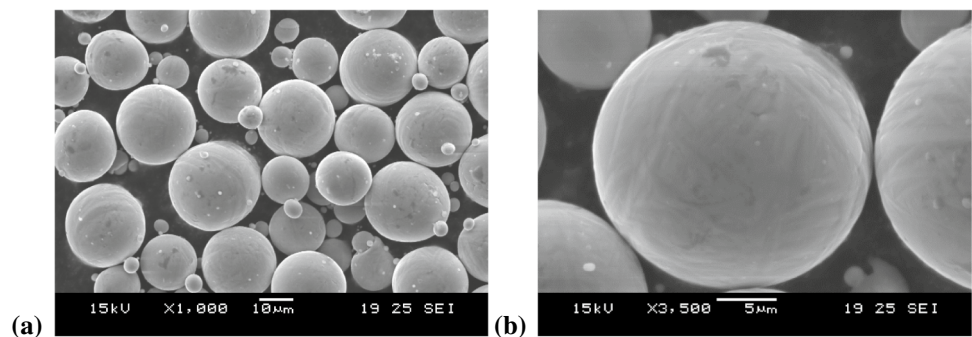


**Table 2** Cold spray deposition details

Parameter	Unit	Sample ID			
		S1	S2	S3	S4
Substrate surface preparation method		Polished	Ground	Sand-blasted	Water-jet cut
Substrate surface roughness, $R_a$	$\mu\text{m}$	0.05	0.3	2.2	5.4
Working gas		Nitrogen			
Gas pressure	MPa	4.5			
Gas temperature	$^{\circ}\text{C}$	950			
Traverse scan speed	mm/s	500			
Spray angle	$^{\circ}$	90			
Stand-off distance	mm	30			
Raster step	mm	1			
No. of passes		10			
Coating thickness per pass	mm	0.15–0.17			
Coating thickness	mm	1.5–1.7			

across the cross section of the sample, and an average hardness value was calculated.

Adhesion strength test was conducted on each coated sample according to the standard ASTM C633 (Ref 41). First, the coated Ti64 sample was slightly ground flat to smoothen the surface while maintaining the original coating thickness. Next, the surface of the sample and stainless steel fixture were sand-blasted with P80 alumina particles, cleaned with ethanol and assembled with an adhesive glue (Araldite AV170, Huntsman Advanced Materials, USA). The assembled set was then placed at a tilt angle of  $35^{\circ}$  in an oven in which the set was cured at  $150^{\circ}\text{C}$  under a weight of 380 g for 60 min and left to cool to room temperature. The set was tested using Instron 5569 (UK), with a load cell of 50 kN in tensile mode at an extension rate of 0.8 mm/min till the set failed.

Interparticle cohesive strength was also tested using mini tensile test in accordance with ASTM E8 (Ref 42). Free standing coatings were fabricated by removing the substrates from the coated samples by using wire cutting. Then, the dog-bone samples were cut from the free standing coatings with the dimensions shown in Fig. 2. The samples were tested using Instron 5569 with an extension speed of 0.3 mm/min until failure (Ref 43). The cohesive stress was calculated by  $F/A$ , where  $F$  is the load and  $A$  is the area of fractured cross section. The cohesive strain was calculated using  $e/L_o$ , where  $e$  is the extension of gauge length and  $L_o$  is the original gauge length.

### Finite Element Modeling

ABAQUS/Explicit, a commercial finite element analysis (FEA) software, was used to simulate individual particle impact on different substrate surface features. Owing to the axisymmetric characteristic of the single particle normal

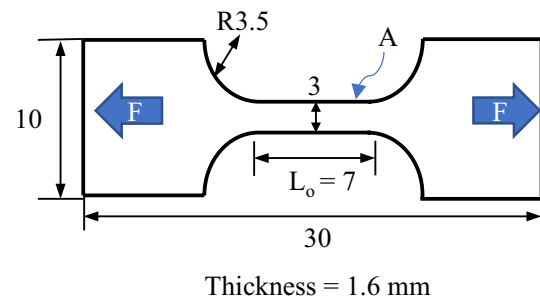
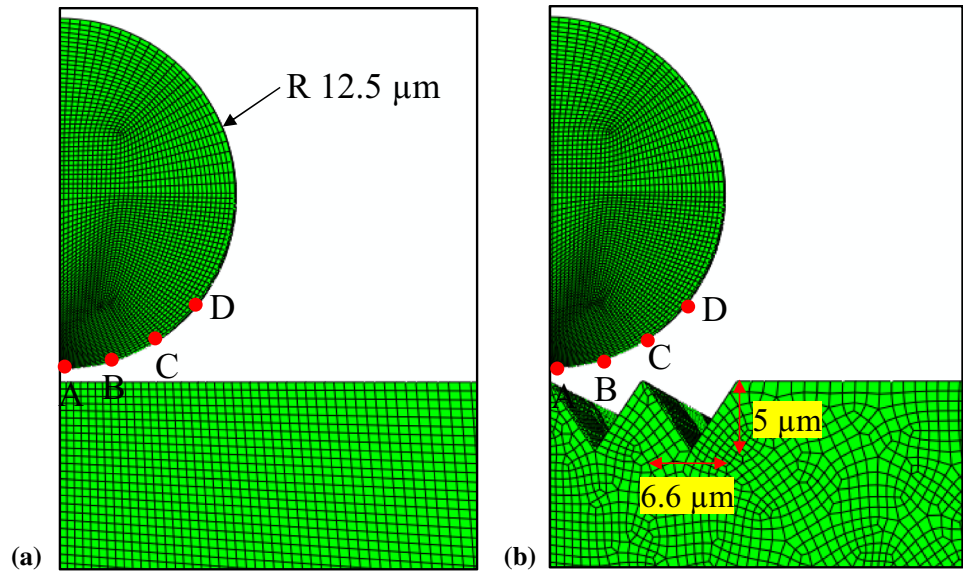


**Fig. 2** Dimensions of dog-bone samples (in mm), where “F” represents the force directions for tensile testing to determine the coating cohesive strength

impact process, one-fourth axisymmetric three-dimensional model is sufficient for the preliminary study on the effect of particle impact on the textured substrate. The diameter of the one-fourth axisymmetric spherical particle ( $d_p$ ) was set to be  $25\ \mu\text{m}$  (taken from the average diameter of powders). In order to reduce the computational time while maintaining the accuracy and reliability of the simulation, the one-fourth axisymmetric square substrate was set to be  $400 \times 400 \times 75\ \mu\text{m}^3$  ( $L \times W \times H$ ). The particle was set at its initial position of  $1\ \mu\text{m}$  above the substrate to ensure the initial separation. The meshing size was kept to  $0.5\ \mu\text{m}$  ( $1/50$  of the particle diameter  $d_p$ ) as the focus is to observe the deformation of the particle and the substrate. An eight-noded hexahedral element with reduced integration and stiffness hourglass control was used as the meshing element as suggested in the literature (Ref 44), and it was verified through several trials. By considering the real situation, the outer side face of the substrate was only allowed to move vertically while the bottom was fixed in all the directions. At the initial stage, the particle and substrate temperatures were set to be 673 K [calculated from Kinetic Spray Solution software (Ref



**Fig. 3** Finite element mesh of a single axisymmetric particle's normal impact onto (a) flat and (b) rough ( $R_a$ : 5  $\mu\text{m}$ ) substrate surfaces



45)] and 573 K (Ref 39), respectively. Besides, the particle was made to impact vertically on the flat (Fig. 3a) and rough ( $R_a$ : 5  $\mu\text{m}$ , similar to water-jet cut) (Fig. 3b) substrate surface at 800 m/s. The details of the material input parameters, model and calculations have been described elsewhere (Ref 16, 46).

## Results and Discussion

### Substrate Surface Analysis

Figure 4 presents the SEM micrographs of each substrate condition and the surface roughnesses  $R_a$  and  $R_z$ . The surface roughnesses (Fig. 5a) obtained for the polished surface is the smoothest ( $R_a$ : 0.05  $\mu\text{m}$ ,  $R_z$ : 0.4), followed by the ground ( $R_a$ : 0.3  $\mu\text{m}$ ,  $R_z$ : 2  $\mu\text{m}$ ), sand-blasted ( $R_a$ : 2.22  $\mu\text{m}$ ,  $R_z$ : 19  $\mu\text{m}$ ) and water-jet cut ( $R_a$ : 5.37  $\mu\text{m}$ ,  $R_z$ : 36.65  $\mu\text{m}$ ) surfaces. Figure 5(a) and (b) show that the SEM image of the polished surface is very smooth, with some signs of scratch marks. The surface profile obtained from 2D line scan in Fig. 5(c) shows the high repetition of peaks and valleys with 0.01  $\mu\text{m}$  roughness width (distance from peak to peak), and fluctuations (peak to valley) of  $\pm 0.2 \mu\text{m}$ .

Figure 5(d) and (e) show that the ground surface has deeper wear tracks with the remaining material from the grinding wheel. The ground surface profile in Fig. 5(f) also shows larger roughness width and fluctuations of 0.02  $\mu\text{m}$  and  $\pm 2 \mu\text{m}$ , respectively. Figure 5(g) and (h) show the SEM micrograph of the sand-blasted surface with the features from erosion by grit impact. The sand-blasted surface consists of lower repetition (in comparison with the polished and ground surfaces) with non-uniform roughness width

of 0.03 to 0.1  $\mu\text{m}$  and fluctuations of 10  $\mu\text{m}$  as shown by the 2D profile shown in Fig. 5(g). Lastly, Fig. 5(j) and (k) shows that the SEM image of the water-jet cut surface has uneven peaks and valleys. The 2D profile in Fig. 5(l) shows the roughness width that can be up to 200  $\mu\text{m}$  and fluctuates around  $\pm 18 \mu\text{m}$ .

The effective surface area would be the question where the surface condition allows optimum contact time and larger attack radius for homogenous bonding—with a jetted ring, which would allow a maximum conversion of kinetic energy to heat, with minimal loss. Kumar et al. (Ref 47) showed that optimum roughness sizes (in terms  $R_z$ ) for soft coating/soft substrate (e.g., Cu/Cu), hard coating/hard substrate (e.g., Ti/Ti64), soft coating/hard substrate (e.g., Al/mild steel) and hard coating/soft substrate (e.g., Ni/Al) are 1, 0.75, 0.5 and 0.75 times of the particle size, respectively. However, such ratios could only be obtained by surface laser texturing (Ref 48), which is challenging for the industry due to (1) time consumption, (2) contamination with air (involving melting of the substrate) and (3) induced residual stresses.

### Coating Surface and Cross-Sectional Analyses

Figure 6(a) and (b) show the overview of the as-sprayed coating surface and a magnified view of particle morphology, respectively. The impacted particles were semi-spherical in shape with material jetting (Fig. 6b, arrow), which means that the particles had sufficient impact energy and underwent adiabatic shear localization bonding. The surface roughness,  $R_a$ , of the as-sprayed coating surface is around 8.6 to 10  $\mu\text{m}$ , which is much higher than the substrate surface roughness (0.05–5.37  $\mu\text{m}$ ). Figure 6(c) shows that a rougher substrate surface slightly increases

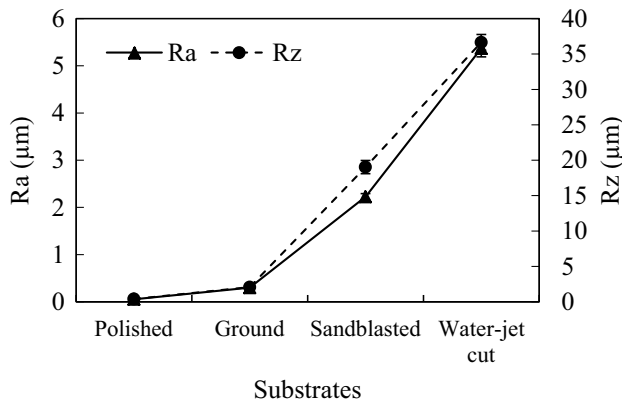


**Fig. 4** Surface roughness ( $R_a$  and  $R_z$ ) as a function of substrate surface condition

the final surface roughness of the coating. The deformation of the particles conforms to the substrate surface profile. The substrate surface profile is projected toward the new coating layer as the layers build up. However, the final projected substrate surface roughness is minimal because the final as-sprayed surface consists of semi-spherical unmelted particles, which is at least 2 times the initial substrate surface roughness.

Figure 7(a-d) show the optical micrographs of the cross sections of the coatings deposited on the substrates with different surface roughnesses. The interface condition does not affect the porosity and hardness of the coatings. In Fig. 7(e), it is observed that the porosity level lies in the range of 4 to 5% and does not change much with an increment of surface roughness. The coatings are relatively dense, although some distinguishable micropores can be noted, which is typical. The average coating hardness is in the range of 350 HV to 400 HV, while the substrate hardness is around 320 HV (Fig. 7f). The etched cross sections in Fig. 8 reveal that the particles underwent severe plastic deformation with varying levels of flatness ratio, due to the momentums of the particles with different sizes and weights. The impact caused the particles to be work-hardened, due to the dislocation movements and dislocation generation within the crystal structure of the material. The surface condition only affects the first interface layer but not subsequent layers, which makes the properties of the coatings similar across the different substrate surface preparations. The phase compositions of the powder feedstock and substrates before the cold spray deposition should be preserved in the coatings and substrates, respectively, after the cold spray deposition, which is based on a similar work reported in the literature (Ref 21, 39).

Figure 8 also shows the coating/substrate interface condition of each coated sample. For the S1 and S2 samples, their interfaces are more intimate as shown in Fig. 8(a) and

(b). Contrary to the S3 and S4 samples shown in Fig. 8(c) and (d), the interfaces are defined with a long continuous succession of microscopic defects in the form of voids and reveal that the deformed coating particles do not follow the substrate surface profiles, which suggests a lack of intimate conformal contact. These voids will then become the source of weakness during the adhesion strength test, which will be shown in the next section. Ti64 alloy is more resistive to plastic deformation due to its HCP crystal structure that has fewer slip systems and a high sensitivity of strain rate hardening where its yield strength increases with increasing strain rate (Ref 49). In comparison, ductile particles such as Cu or Al adhere better to rough surfaces as they can conform and mechanically anchor to the increased surface areas of rough surfaces with formation of interfacial roll-ups and vortices (Ref 50). In addition, the impact of the particles on a textured surface may have caused the particles and the substrate sub-surface to shatter (Fig. 8c and d), forming a weak layer that becomes a source of failure.

### Adhesion and Cohesion Analyses

Coating adhesion strength is one of the important measures for evaluating the bonding quality of the CS coating on the substrate. Figure 9 shows the effect of surface roughness on the adhesion strength of the coating to the substrate. Figure 9(a) demonstrates that the adhesion strength of the coatings significantly reduces with increasing substrate surface roughness. The S1 sample has managed to obtain glue failure as shown in Fig. 9(b) with the coating adhesion strength exceeded 68.7 MPa. As for the S2, S3 and S4 samples, they all have suffered coating/substrate interface failure with the bond strengths of 44.8, 7.5 and 7.14 MPa, respectively. When the coating is subjected to an increase in tensile load during the adhesion test, cracks and detachments often happen in the weakly bonded regions, for example, in the S4 sample, which reveals that a rough surface profile prevents adequate metal jetting and effective bonding, which will be shown in the modeling section later. In addition, some glue stains are present at the periphery of a poorly bonded interface (Fig. 9c), which may have flowed into the interface during curing, since the coating may have some prior delamination during the CS process.

Another reason for an interface or a glue failure to occur is because the coating cohesive strength is much higher than the interface strength. The interparticle strength of the three samples is around 350 MPa before failure, attaining a strain of around 4 to 5% as shown in Fig. 10(a). The failure mode is a brittle failure as there are no signs of plasticity such as hardening and necking after the yield point (Fig. 10b). In comparison with bulk Ti64 grade 5, the ultimate tensile strength is around 895-930 MPa and the strain is around 6 to

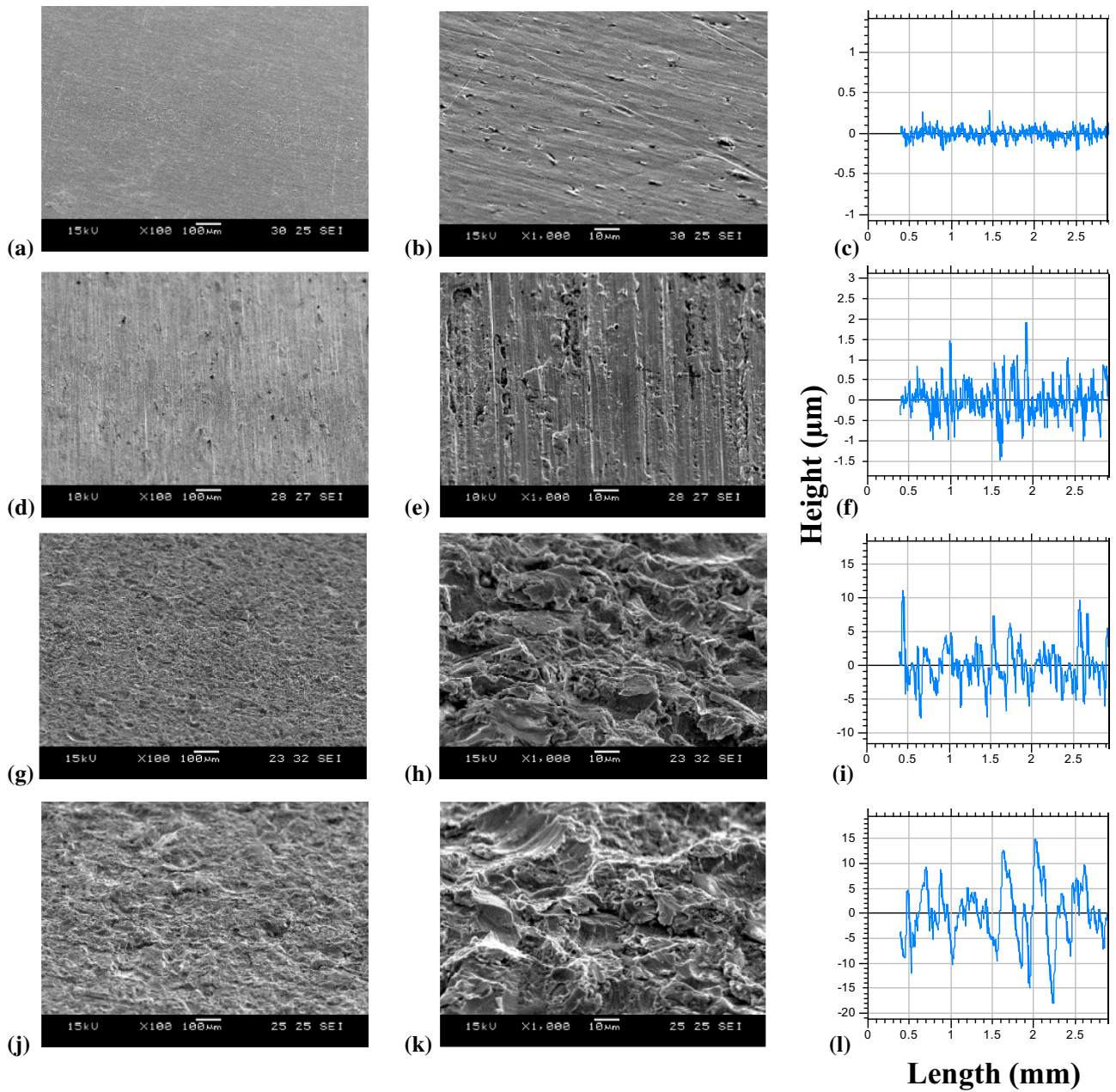


**Fig. 5** SEM micrographs taken at a 60° tilt angle for lower (left column) and higher (middle column) magnifications, and 2D surface profiles (right column) for (a-c) polished, (d-f) ground, (g-i) sand-blasted and (j-l) water-jet cut, respectively

10% (Ref 51). Therefore, as a CS coating, it has a considerable high amount of cohesive strength. In comparison, CS Ti coatings were reported to have a cohesive strength of around 300 MPa (Ref 19), which is slightly lower. This result shows that the interface layer does not affect the quality of the subsequent build-up layer of the coating, as discussed earlier. The cohesive strength results also show that the preferred crack propagation direction would be across the interface as it is the path of least resistance for the release of stress when being under a tensile load.

### Fractography

The coating/substrate interface fracture patterns after the adhesion tests are examined for both coating and substrate sides, as shown in Fig. 11. For the S2 substrate surface, craters and adhered particles are observed in Fig. 11(a). A crater center has a smoother surface as the shear instabilities only occur at the periphery of the particles, i.e., jetted regions. Some of the craters have broken pieces of the jetted section of the particle. This occurs because a



**Fig. 6** (a and b) SEM micrographs of the as-sprayed surface at different magnifications; and (c) coating surface roughness as a function of substrate surface roughness

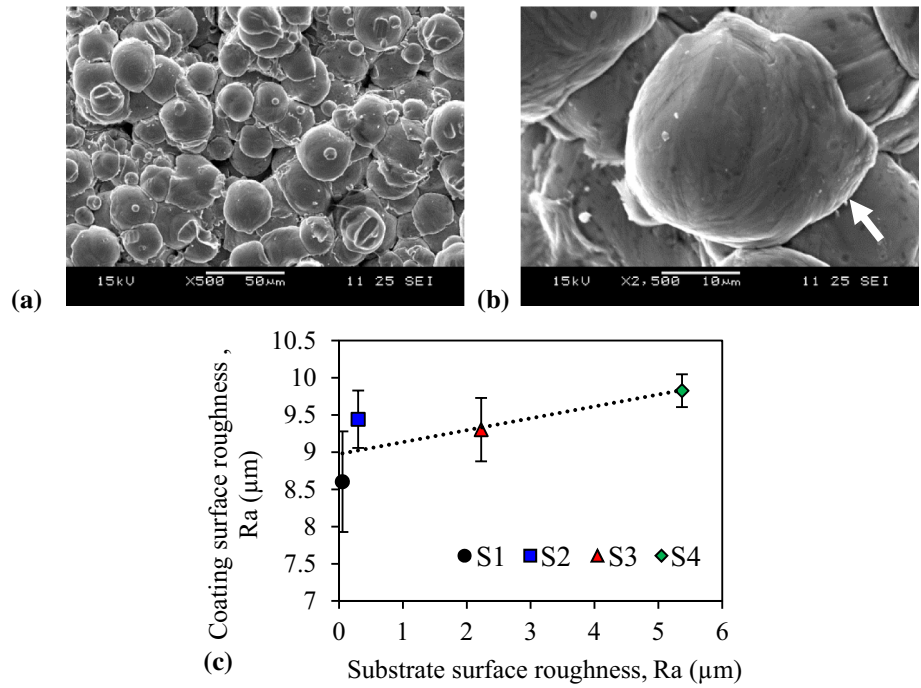


**Fig. 7** (a-d) Optical micrographs of polished cross sections, (e) porosity and (f) hardness for coatings as a function of substrate surface roughness. The arrows indicate the interfaces between coatings and substrates

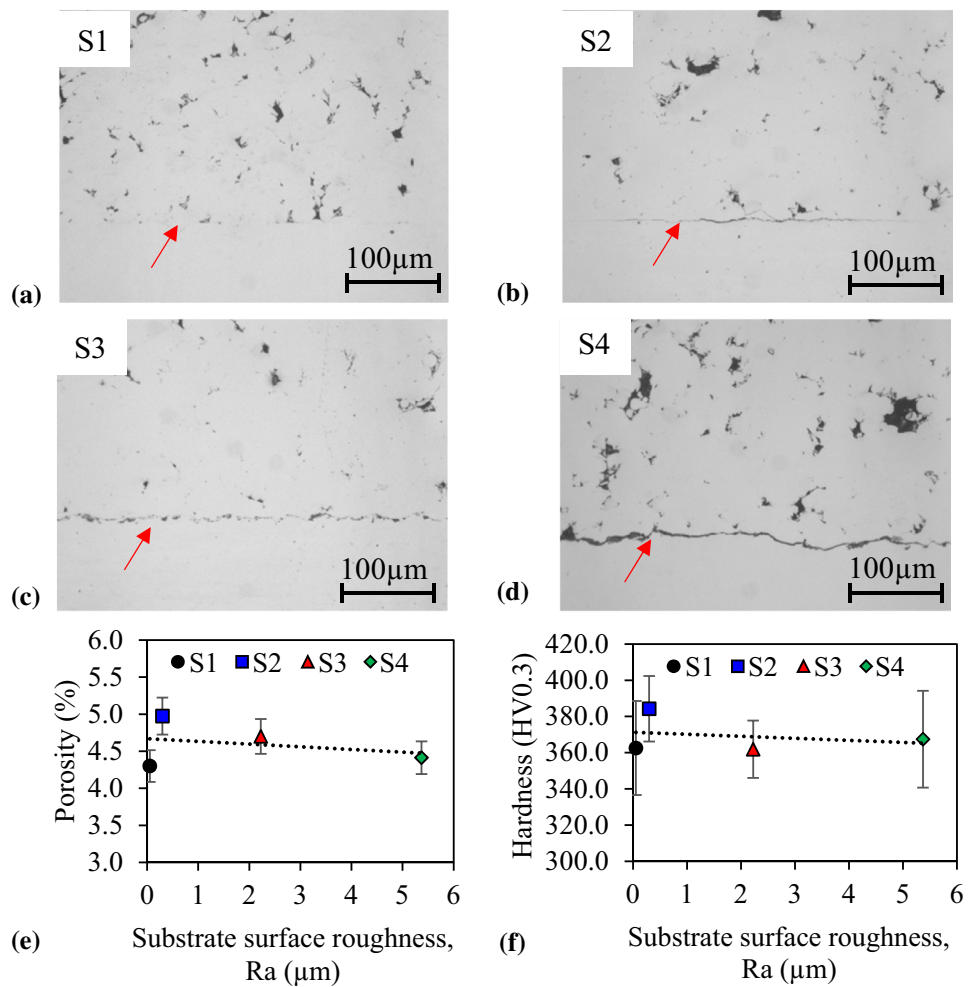
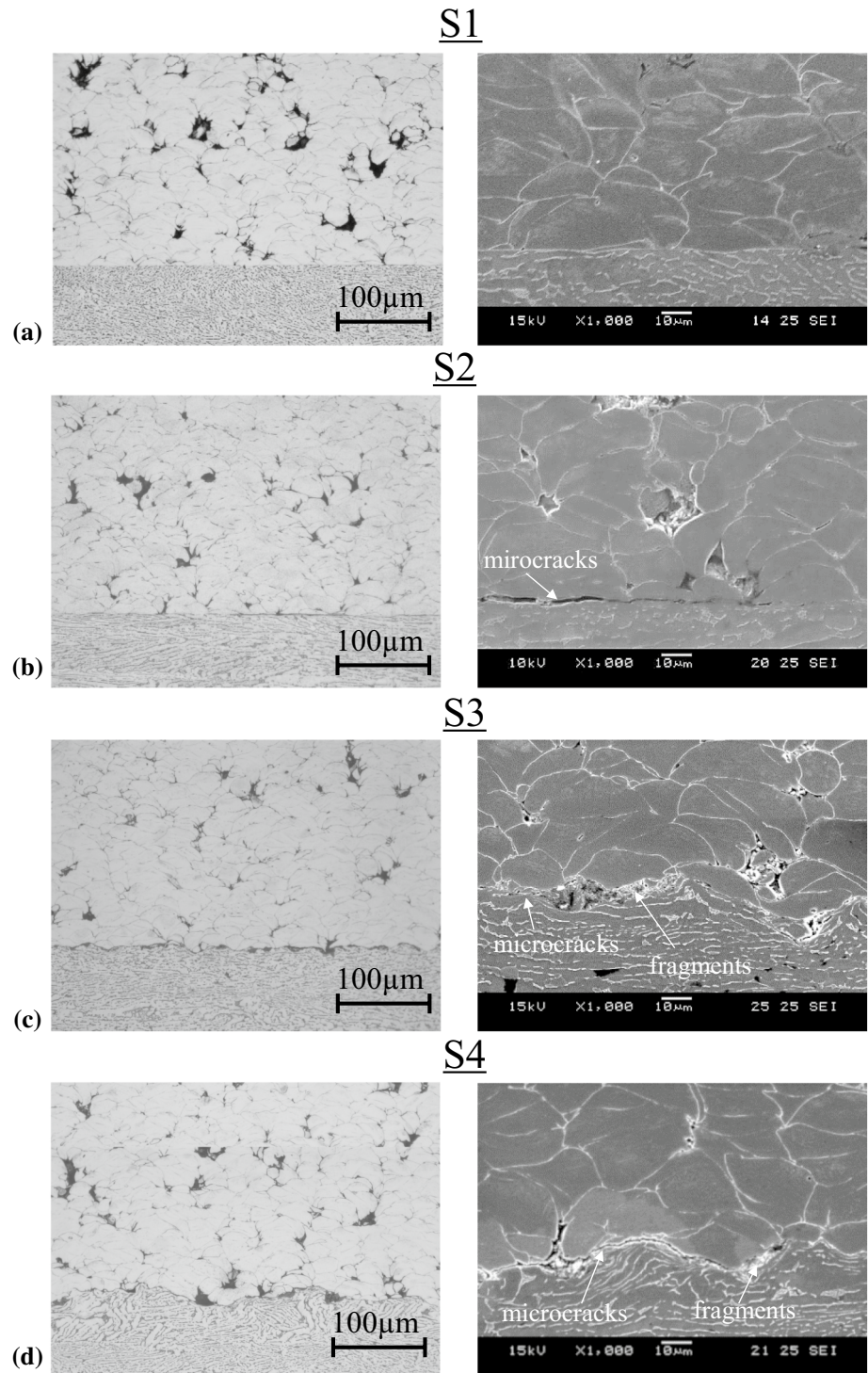


**Fig. 8** (a-d) Optical (left) and SEM (right) micrographs of etched cross sections for coatings deposited on substrates with different surface roughnesses



jetted region consists of refined grains which are more brittle (Ref 21, 52). The coating side consists of the protruded particles due to the penetration of the particles into the substrate. Some protrusions have dimple fracture due to detachment of the jetted region. Such dimple fracture patterns are indications of strong adhesion (metallurgical bonding) because a higher force would be required to break

a particle cohesively as compared to its bonding interface. In addition, such features also show that a strong adhesion may be localized and not uniform across the entire jetted region. It is believed that the interface condition of the S1 surface would have similar features with S2, except with more craters and remains of the jetted area, if failure occurs [shown elsewhere (Ref 21)].



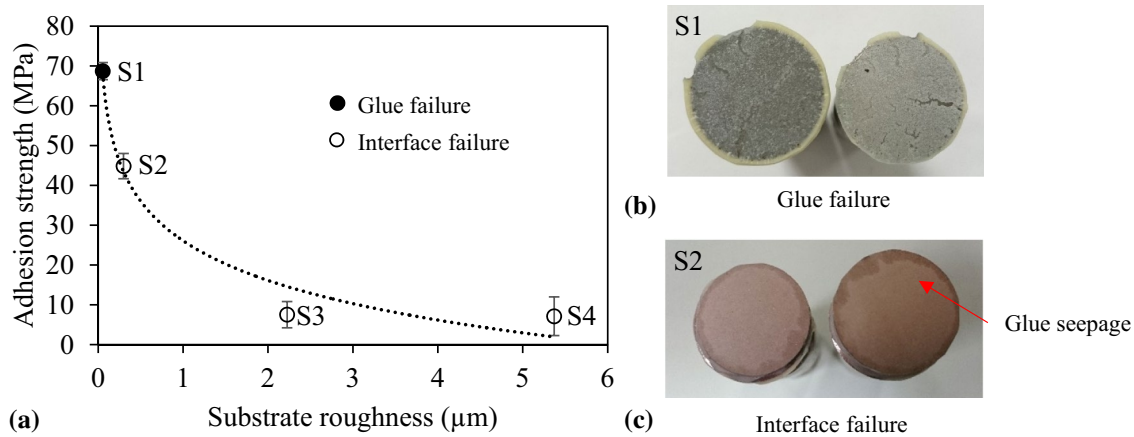


**Fig. 9** (a) Adhesion strength as a function of substrate surface roughness and (b and c) photographs of (b) glue and (c) interface failure

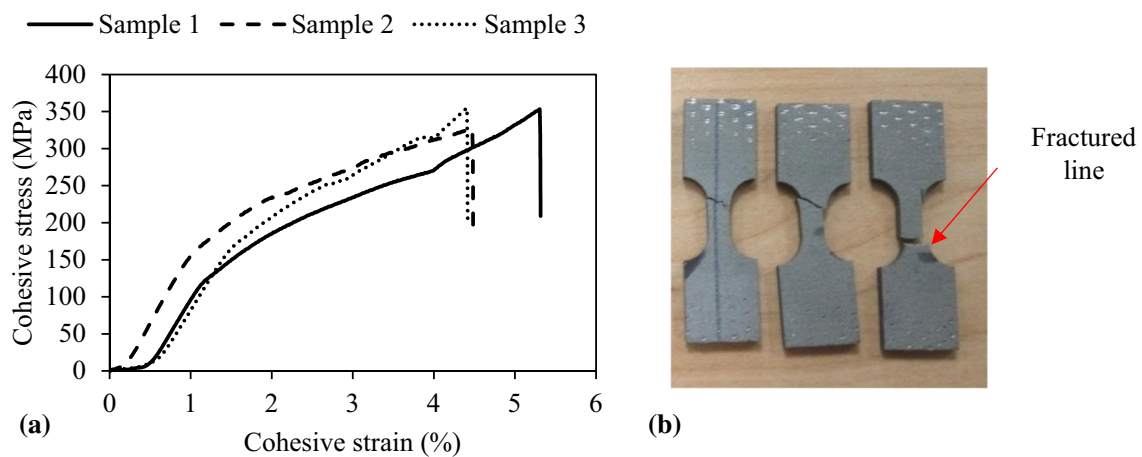


**Fig. 10** (a) Cohesive strength as a function of cohesive strain and (b) photograph of cohesively fractured samples

For the S3 (Fig. 11b) and S4 (Fig. 11c) samples, individual protrusions or craters are harder to observe as the deformation of the particles conforms to the surface texture. The substrate undergoes minimal deformation during the deposition process because the general texture appears to be the same as that before deposition, and the morphology is still characterized by grit-shaped dents, increasing in size with the substrate surface roughness. There are also fewer particles that remain adhered to the surface due to weak bonding, which will be further discussed in the modeling section.

Figure 12(a) shows an overview of the fractured cross section of the cohesively tested sample. Figure 12(b) (arrow) shows some of the particles debonded completely (without dimples) from the neighboring particles due to poor particle–particle bonding. On the other hand, some particles have dimples (Fig. 12b, circle) belonging to the fragments of the debonded Ti64 particles (cohesively broken), which are left adhered on the particle surfaces. This is an indication of a strong bonding, where the

interparticle interface strength has exceeded the particle cohesive strength, which accounts for the high cohesive strength.

### Impact Simulation on Different Surface Roughnesses

The particle impact onto a textured substrate surface is modeled as the time-evolution of temperature, stress and strain, which cannot be captured experimentally. In the modeling of this study, a flat surface and a rough surface ( $R_a: 5 \mu\text{m}$ ) are used to represent a polished surface and a water-jet cut surface, respectively. As depicted in Fig. 13(a) and (b), the particle impact at a critical velocity (Ref 46) on the flat surface shows that the particle is able to form a material jet at the periphery. This can be attributed to the ASI, where the accumulation of heat (from 673 to 1534 K as shown in Fig. 14a), reduction in flow stress (from 839 to 318 MPa as shown in Fig. 14b) and increase in strain (from 0 to 683% as shown in Fig. 14c) take place most extensively and uniformly at the periphery of the particle [based on element D

**Fig. 11** SEM micrographs of interface failure (coating and substrate side) for (a) S2, (b) S3 and (c) S4 samples at 45° tilt angle

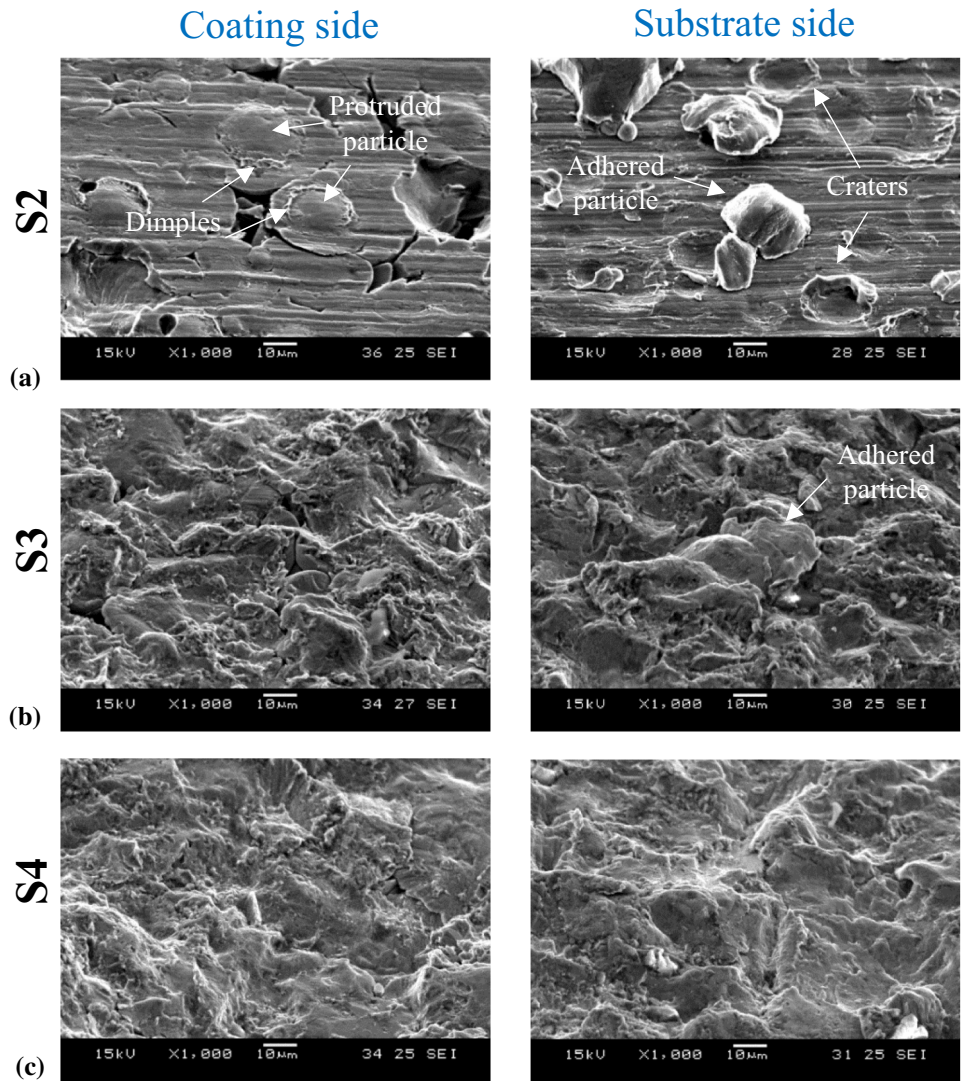
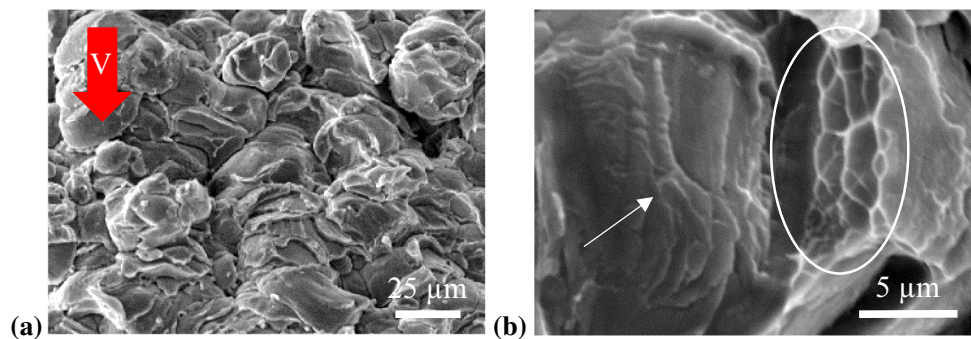


**Fig. 12** SEM micrographs of cohesive failure for (a) overview and (b) enlarged view of fractured surface with smooth (arrow) and dimple fractures (circle). The arrow “V” in (a) indicates the particle impact direction



in Fig. 13(a) and (b)]. The substrate deformation and temperature distribution from the particle impact on the substrate have a similar trend with the particle as shown in Fig. 13(c). Such phenomena would enable strong bonding between the particle and substrate, and achieve a high adhesion strength of more than 68.7 MPa, as shown in Fig. 9. The stress and

strain (PEEQ) distributions in the particle and substrate are shown in Figure SI-1 in the Supplementary Information.

On the other hand, Fig. 13(d) and (e) show that the particle impacted onto the rough surface demonstrates a significant impediment for the formation of material jetting, as a result of non-uniform heat and strain distributions. The

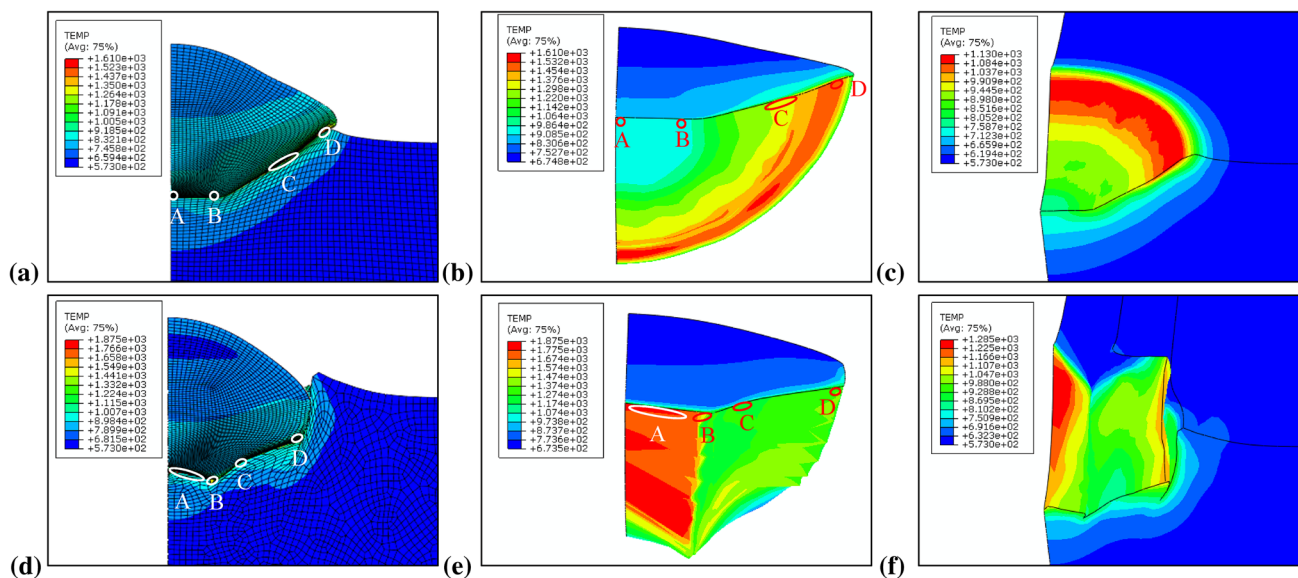


**Fig. 13** FEM models established after particle impact on (a-c) flat surface and (d-f) rough surface at 28 ns, where (a and d) are front view, (b and e) particle front and bottom, and (c and f) crater on the substrate. The elements A to D are deformed upon impact

particle impact onto the peak section (element A) reveals a significant increase in temperature (from 673 to 1818 K as shown in Fig. 14d), drop in flow stress (from 846 to 44 MPa as shown in Fig. 14e) and increase in strain (0 to 1560% as shown in Fig. 14f). However, these effects are less significant when the particle impacts the valley section, for example, for element B where the changes in temperature, stress and strain are 673 to 1287 K (Fig. 14d), 842 to 523 MPa (Fig. 14e) and 0 to 423% (Fig. 14f), respectively. In Fig. 13(f), the substrate also shows that the peak and valley features are deformed, as energy is used to deform the surface features instead of bonding, as evidenced by lack of dimple fracture in the fractography (Fig. 11b and c). The combined effect of uneven temperature (Fig. 13e and f), stress (Figure SI-2a and b in Supplementary Information) and strain (Figure SI-2c and d in Supplementary Information) distributions along the particle base and substrate result in uneven bonding, which will lead to higher interfacial stresses and cracks as shown in Fig. 8(c) and (d) that possibly promote the debonding of the coating from the substrate.

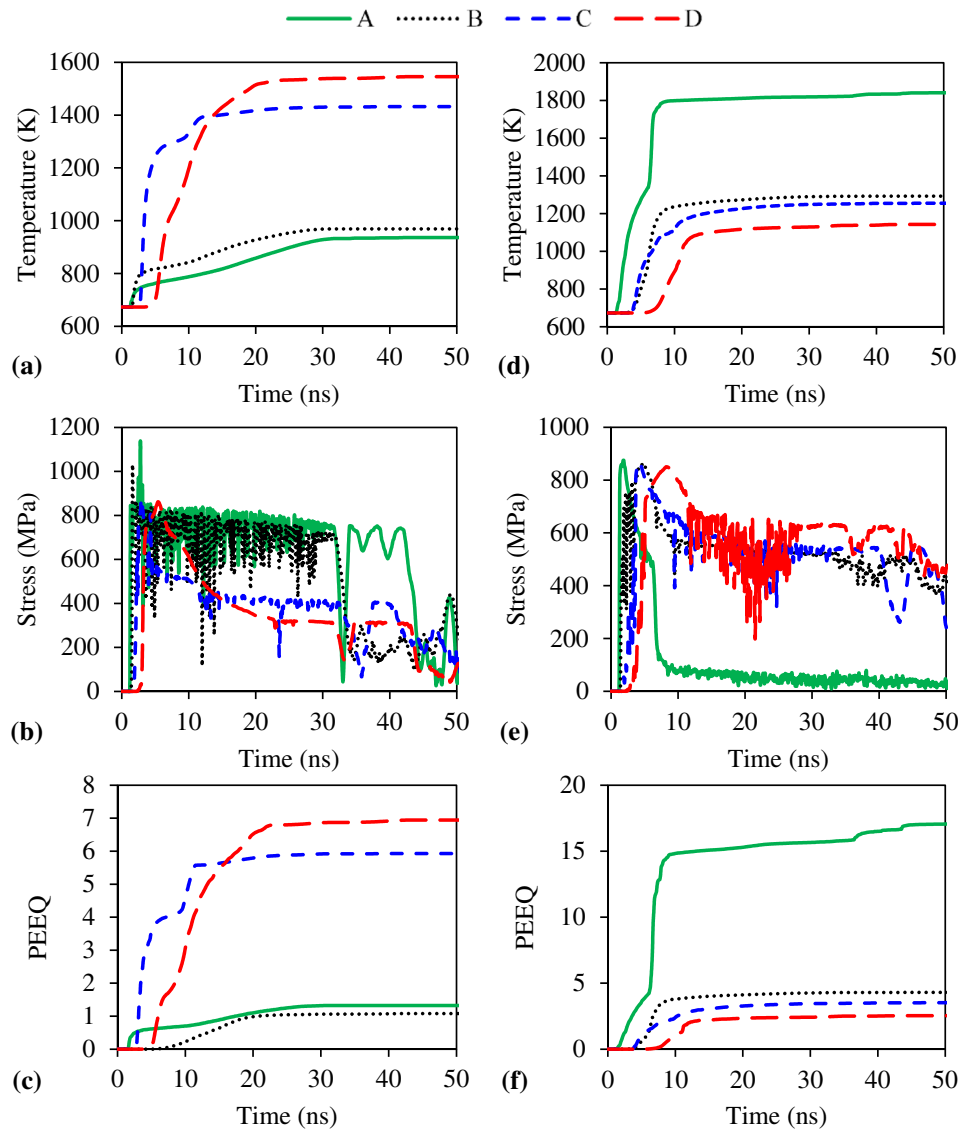
## Conclusions

The deposition of CS Ti64 coatings on Ti64 substrates with different surface roughnesses was investigated by means of both experimental and numerical methods, which led to a deeper understanding on the microstructure and mechanical properties of the coatings. Based on the results obtained from the study, the following conclusions were drawn:

1. Different substrate surface preparations would influence the surface roughness profile in terms of amplitude and width. The substrate surface roughness had minimal impact on the final coating surface roughness ( $R_a$ : 8.6–10  $\mu\text{m}$ , mainly contributed by semi-spherical particles), porosity (4–5%) and hardness (350–400 HV).
2. The interfaces between the CS Ti64 coatings and smoother substrates ( $R_a$ : 0.05 and 0.3  $\mu\text{m}$ ) were more intimate due to the lack of microscopic defects and cracks than the coatings on the rougher substrates ( $R_a$ : 2.2 and 5.4  $\mu\text{m}$ ). A higher substrate surface roughness acted as a barrier for the particles to undergo strain localization with the substrate surface upon impact.
3. The adhesion strength of the CS Ti64 coating deposited on the smoothest substrate surface ( $R_a$ : 0.05  $\mu\text{m}$ ) exceeded 68.9 MPa (glue failure), while the CS Ti64 coatings on the rough substrate surfaces ( $R_a$ : 2.2 and 5.4  $\mu\text{m}$ ) yielded low adhesion strengths, around 7 to 7.5 MPa. Fractography of the coating/substrate (with interface failure) revealed that a smooth substrate surface had more ASI-induced craters (dimple fractures) as compared to the rough surfaces, as an indication of stronger metallurgical bonding.
4. Finite element modeling showed that the impact of a particle onto a rough substrate surface ( $R_a$ : 5  $\mu\text{m}$ ) prevented intimate bonding owing to the non-uniform distributions of strain and temperature at the particle/substrate interface, as compared to a smooth substrate surface.



**Fig. 14** Temporal evolutions of temperature, stress (von Mises) and PEEQ (equivalent plastic strain) for elements A, B, C and D during particle impact on (a-c) flat and (d-f) rough surfaces, respectively



**Acknowledgments** This work was financially supported by the National Research Foundation (NRF), Rolls-Royce (RR) and Nanyang Technological University (NTU), Singapore, with the research grant (ARMS 1.1 Advanced metalized coatings using cold spray project).

**References**

1. R.R. Boyer, An Overview on the Use of Titanium in the Aerospace Industry, *Mater. Sci. Eng., A*, 1996, **213**(1), p 103-114
2. A. Papyrin, V. Kosarev, S. Klinkov, A. Alkhimov, and V.M. Fomin, *Cold Spray Technology*, Elsevier, Amsterdam, 2007
3. R.C. Dykhuizen, M.F. Smith, D.L. Gilmore, R.A. Neiser, X. Jiang, and S. Sampath, Impact of High Velocity Cold Spray Particles, *J. Therm. Spray Technol.*, 1999, **8**(4), p 559-564
4. J. Vlcek, L. Gimeno, H. Huber, and E. Lugscheider, A Systematic Approach to Material Eligibility for the cold-Spray Process, *J. Therm. Spray Technol.*, 2005, **14**(1), p 125-133
5. R.C. McCune, A.N. Papyrin, J.N. Hall, W.L. Riggs II, P.H. Zajchowski, An Exploration of the cold-gas-dynamic spray method for several materials systems, *Advances in Thermal Spray Science and Technology*, C.C. Berndt, S. Sampath, Eds., ASM International, Materials Park, p 1 (1995)
6. V.F. Kosarev, S.V. Klinkov, A.P. Alkhimov, and A.N. Papyrin, On Some Aspects of Gas Dynamics of the Cold Spray Process, *J. Therm. Spray Technol.*, 2003, **12**(2), p 265-281
7. T. Schmidt, F. Gaertner, and H. Kreye, New Developments in Cold Spray Based on Higher Gas and Particle Temperatures, *J. Therm. Spray Technol.*, 2006, **15**(4), p 488-494
8. M. Grujcic, C.L. Zhao, W.S. DeRosset, and D. Helfritsch, Adiabatic Shear Instability Based Mechanism for particles/Substrate Bonding in the Cold-Gas Dynamic-Spray Process, *Mater. Des.*, 2004, **25**(8), p 681-688
9. G. Bae, S. Kumar, S. Yoon, K. Kang, H. Na, H.J. Kim, and C. Lee, Bonding Features and Associated Mechanisms in Kinetic Sprayed Titanium Coatings, *Acta Mater.*, 2009, **57**(19), p 5654-5666
10. G. Bae, Y. Xiong, S. Kumar, K. Kang, and C. Lee, General Aspects of Interface Bonding in Kinetic Sprayed Coatings, *Acta Mater.*, 2008, **56**(17), p 4858-4868
11. M. Perton, S. Costil, W. Wong, D. Poirier, E. Irissou, J.G. Legoux, A. Blouin, and S. Yue, Effect of Pulsed Laser Ablation

- and Continuous Laser Heating on the Adhesion and Cohesion of Cold Sprayed Ti-6Al-4V Coatings, *J. Therm. Spray Technol.*, 2012, **21**(6), p 1322-1333
12. W. Sun, A.W.Y. Tan, A. Bhowmik, I. Marinescu, X. Song, W. Zhai, F. Li, and E. Liu, Deposition Characteristics of Cold Sprayed Inconel 718 Particles on Inconel 718 Substrates with Different Surface Conditions, *Mater. Sci. Eng., A*, 2018, **720**, p 75-84
  13. W. Sun, A.W.Y. Tan, N.W. Khun, I. Marinescu, and E. Liu, Effect of Substrate Surface Condition on Fatigue Behavior of Cold Sprayed Ti6Al4V Coatings, *Surf. Coat. Technol.*, 2017, **320**, p 452-457
  14. P. Cavaliere and A. Silvello, Processing Parameters Affecting Cold Spray Coatings Performances, *The International Journal of Advanced Manufacturing Technology*, 2013, **71**(1-4), p 263-277
  15. V.S. Bhattiprolu, K.W. Johnson, O.C. Ozdemir, and G.A. Crawford, Influence of Feedstock Powder and Cold Spray Processing Parameters on Microstructure and Mechanical Properties of Ti-6Al-4V cold Spray Depositions, *Surf. Coat. Technol.*, 2018, **335**, p 1-12
  16. A.W.Y. Tan, J.Y. Lek, W. Sun, A. Bhowmik, I. Marinescu, X. Song, W. Zhai, F. Li, Z. Dong, C. Boothroyd, and E. Liu, Influence of Particle Velocity When Propelled Using N<sub>2</sub> or N<sub>2</sub>-He Mixed Gas on the Properties of Cold-Sprayed Ti6Al4V Coatings, *Coatings*, 2018, **8**(9), p 327
  17. D. Goldbaum, J.M. Shockley, R.R. Chromik, A. Rezaeian, S. Yue, J.G. Legoux, and E. Irissou, The Effect of Deposition Conditions on Adhesion Strength of Ti and Ti6Al4V Cold Spray Splats, *J. Therm. Spray Technol.*, 2011, **21**(2), p 288-303
  18. N.W. Khun, A.W.Y. Tan, K.J.W. Bi, and E. Liu, Effects of Working Gas on Wear and Corrosion Resistances of Cold Sprayed Ti-6Al-4V Coatings, *Surf. Coat. Technol.*, 2016, **302**, p 1-12
  19. K. Binder, J. Gottschalk, M. Kollenda, F. Gärtner, and T. Klassen, Influence of Impact Angle and Gas Temperature on Mechanical Properties of Titanium Cold Spray Deposits, *J. Therm. Spray Technol.*, 2010, **20**(1-2), p 234-242
  20. N.W. Khun, A.W.Y. Tan, W. Sun, and E. Liu, Wear and Corrosion Resistance of Thick Ti-6Al-4V Coating Deposited on Ti-6Al-4V Substrate via High-Pressure Cold Spray, *J. Therm. Spray Technol.*, 2017, **26**(6), p 1393-1407
  21. A.W.-Y. Tan, W. Sun, A. Bhowmik, J.Y. Lek, I. Marinescu, F. Li, N.W. Khun, Z. Dong, and E. Liu, Effect of Coating Thickness on Microstructure, Mechanical Properties and Fracture Behaviour of Cold Sprayed Ti6Al4V Coatings on Ti6Al4V Substrates, *Surf. Coat. Technol.*, 2018, **349**, p 303-317
  22. N.W. Khun, A.W.Y. Tan, W. Sun, and E. Liu, Effects of Nd:YAG Laser Surface Treatment on Tribological Properties of Cold-Sprayed Ti-6Al-4V Coatings Tested against 100Cr6 Steel under Dry Condition, *Tribol. Trans.*, 2019, **62**(3), p 391-402
  23. N.W. Khun, A.W.Y. Tan, W. Sun, and E. Liu, Effect of Heat Treatment Temperature on Microstructure and Mechanical and Tribological Properties of Cold Sprayed Ti-6Al-4V Coatings, *Tribol. Trans.*, 2016, **60**, p 1-10
  24. T. Samson, D. MacDonald, R. Fernández, and B. Jodoin, Effect of Pulsed Waterjet Surface Preparation on the Adhesion Strength of Cold Gas Dynamic Sprayed Aluminum Coatings, *J. Therm. Spray Technol.*, 2015, **24**(6), p 984-993
  25. R. Fernández, D. MacDonald, A. Nastić, B. Jodoin, A. Tieu, and M. Vijay, Enhancement and Prediction of Adhesion Strength of Copper Cold Spray Coatings on Steel Substrates for Nuclear Fuel Repository, *J. Therm. Spray Technol.*, 2016, **25**(8), p 1577-1587
  26. T. Hussain, D.G. McCartney, P.H. Shipway, and D. Zhang, Bonding Mechanisms in Cold Spraying: The Contributions of Metallurgical and Mechanical Components, *J. Therm. Spray Technol.*, 2009, **18**(3), p 364-379
  27. Q. Blochet, F. Delloro, F. N'Guyen, D. Jeulin, F. Borit, and M. Jeandin, Effect of the Cold-Sprayed Aluminum Coating-Substrate Interface Morphology on Bond Strength for Aircraft Repair Application, *J. Therm. Spray Technol.*, 2017, **26**(4), p 671-686
  28. S.I. Imbriglio, N. Brodusch, M. Aghasibeig, R. Gauvin, and R.R. Chromik, Influence of Substrate Characteristics on Single Ti Splat Bonding to Ceramic Substrates by Cold Spray, *J. Therm. Spray Technol.*, 2018, **27**(6), p 1011-1024
  29. S. Theimer, M. Graunitz, M. Schulze, F. Gaertner, and T. Klassen, Optimization Adhesion in Cold Spraying onto Hard Substrates: A Case Study for Brass Coatings, *J. Therm. Spray Technol.*, 2019, **28**(1-2), p 124-134
  30. T. Marrocco, D.G. McCartney, P.H. Shipway, and A.J. Sturgeon, Production of Titanium Deposits by Cold-Gas Dynamic Spray: Numerical Modeling and Experimental Characterization, *J. Therm. Spray Technol.*, 2006, **15**(2), p 263-272
  31. J. Wu, J. Yang, H. Fang, S. Yoon, and C. Lee, The Bond Strength of Al-Si Coating on Mild Steel by Kinetic Spraying Deposition, *Appl. Surf. Sci.*, 2006, **252**(22), p 7809-7814
  32. H. Mäkinen, J. Lagerbom, P. Vuoristo, Adhesion of Cold Sprayed Coatings: Effect of Powder, Substrate, and Heat Treatment, *Thermal Spray: Global Coating Solutions*, B.R. Marple, M.M. Hyland, Y. Lau, C. Li, R.S. Lima, G. Montavon, Eds., May 14-16, 2007 (Beijing, People's Republic of China), ASM International, 2007, p 31-36
  33. K. Sakaki, T. Tajima, H. Li, S. Shinkai, Y. Shimizu, Influence of Substrate Conditions and Traverse Speed on Cold Sprayed Coatings, ITSC 2004: International Thermal Spray Conference 2004: Advances in Technology and Application, pp 358-362 (2004)
  34. P. Richer, B. Jodoin, K. Taylor, E. Sansoucy, M. Johnson, L. Ajdelsztajn, Effect of Particle Geometry and Substrate Preparation in Cold Spray, *Therm. Spray 2005: Explore Surf. Potential*, 2-4 (2005)
  35. H.-R. Wang, B.-R. Hou, J. Wang, Q. Wang, and W.-Y. Li, Effect of Process Conditions on Microstructure and Corrosion Resistance of Cold-Sprayed Ti Coatings, *J. Therm. Spray Technol.*, 2008, **17**(5-6), p 736-741
  36. W.-Y. Li, C. Zhang, X. Guo, C.-J. Li, H. Liao, and C. Coddet, Study on Impact Fusion at Particle Interfaces and Its Effect on Coating Microstructure in Cold Spraying, *Appl. Surf. Sci.*, 2007, **254**(2), p 517-526
  37. T.S. Price, P.H. Shipway, and D.G. McCartney, Effect of Cold Spray Deposition of a Titanium Coating on Fatigue Behavior of a Titanium Alloy, *J. Therm. Spray Technol.*, 2006, **15**(4), p 507-512
  38. W. Wong, A. Rezaeian, E. Irissou, J.G. Legoux, and S. Yue, Cold spray characteristics of commercially pure Ti and Ti-6Al-4V, *Advanced Materials Research*, T. Chandra, N. Wanderka, W. Reimers, and M. Ionescu, Ed., Trans Tech Publ, Zurich, 2010, p 639-644
  39. A.W.-Y. Tan, W. Sun, Y.P. Phang, M. Dai, I. Marinescu, Z. Dong, and E. Liu, Effects of Traverse Scanning Speed of Spray Nozzle on the Microstructure and Mechanical Properties of Cold-Sprayed Ti6Al4V Coatings, *J. Therm. Spray Technol.*, 2017, **26**(7), p 1484-1497
  40. A.M. Birt, V.K. Champagne, R.D. Sisson, and D. Apelian, Microstructural Analysis of Cold-Sprayed Ti-6Al-4V at the Micro- and Nano-Scale, *J. Therm. Spray Technol.*, 2015, **24**(7), p 1277-1288
  41. ASTM International, *ASTM C633-13, Standard Test Method for Adhesion or Cohesion Strength of Thermal Spray Coatings*, ASTM International, West Conshohocken, 2013
  42. ASTM International, *ASTM E8/E8 M-13, Standard Test Methods for Tension Testing of Metallic Materials*, ASTM International, West Conshohocken, 2013
  43. W. Sun, A. Bhowmik, A.W.Y. Tan, F. Xue, I. Marinescu, F. Li, and E. Liu, Strategy of Incorporating Ni-Based Braze Alloy in Cold Sprayed Inconel 718 Coating, *Surf. Coat. Technol.*, 2019, **358**, p 1006-1012



44. W.-Y. Li and W. Gao, Some Aspects on 3D Numerical Modeling of High Velocity Impact of Particles in Cold Spraying by Explicit Finite Element Analysis, *Appl. Surf. Sci.*, 2009, **255**(18), p 7878-7892
45. <https://kinetic-spray-solutions.com/>. Accessed 19 Jan 2018
46. X. Song, J. Everaerts, W. Zhai, H. Zheng, A.W.Y. Tan, W. Sun, F. Li, I. Marinescu, E. Liu, and A.M. Korsunsky, Residual Stresses in single Particle Splat of Metal Cold Spray Process—Numerical Simulation and Direct Measurement, *Mater. Lett.*, 2018, **230**, p 152-156
47. S. Kumar, G. Bae, and C. Lee, Influence of Substrate Roughness on Bonding Mechanism in Cold Spray, *Surf. Coat. Technol.*, 2016, **304**, p 592-605
48. R. Kromer, S. Costil, C. Verdy, S. Gojon, and H. Liao, Laser Surface Texturing to Enhance Adhesion Bond Strength of Spray Coatings—Cold Spraying, Wire-Arc Spraying, and atmospheric Plasma Spraying, *Surf. Coat. Technol.*, 2017, **352**, p 642-653
49. R.S. Yatnalkar, *Experimental Investigation of Plastic Deformation of Ti-6Al-4V Under Various Loading Conditions*, The Ohio State University, Columbus, 2010
50. R. Singh, K.H. Rauwald, E. Wessel, G. Mauer, S. Schrufer, A. Barth, S. Wilson, and R. Vassen, Effects of Substrate Roughness and Spray-Angle on Deposition Behavior of Cold-Sprayed Inconel 718, *Surf. Coat. Technol.*, 2017, **319**, p 249-259
51. M. Niinomi, Mechanical Properties of Biomedical Titanium Alloys, *Mater. Sci. Eng., A*, 1998, **243**(1), p 231-236
52. J.Y. Lek, A. Bhowmik, A.W.-Y. Tan, W. Sun, X. Song, W. Zhai, P.J. Buenconsejo, F. Li, E. Liu, Y.M. Lam, and C.B. Boothroyd, Understanding the Microstructural Evolution of Cold Sprayed Ti-6Al-4V Coatings on Ti-6Al-4V Substrates, *Appl. Surf. Sci.*, 2018, **459**, p 492-504

**Publisher's Note** Springer Nature remains neutral with regard to jurisdictional claims in published maps and institutional affiliations.